Precision Engineering 55 (2019) 1–13

Contents lists available at ScienceDirect

Precision Engineering

journal homepage: www.elsevier.com/locate/precision

Milling bifurcations for strongly asymmetric, symmetric, and weakly asymmetric system dynamics

Andrew Honeycutt, Tony Schmitz*

University of North Carolina at Charlotte, Mechanical Engineering and Engineering Science, Charlotte, NC, USA

ARTICLE INFO

Keywords:
Milling
Dynamics
Chatter
Bifurcation

ABSTRACT

This paper uses time domain simulation to predict milling behavior for three distinct dynamic system configurations: 1) strongly asymmetric; 2) symmetric; and 3) weakly asymmetric. These correspond to physical setups that include: 1) a single degree-of-freedom flexure used to simplify in-process metrology for model validation; 2) long, flexible endmill dynamics; and 3) tool or workpiece-dominated dynamics with weak asymmetry in the plane of the cut. The time domain simulation displacement and velocity outputs are sampled at the tooth period to produce Poincaré maps and subharmonic sampling is combined with a numerical stability metric to produce stability maps. These Poincaré and stability maps are used to characterize the milling behavior and identify period-n bifurcations. Experimental validation is provided for the flexure-based setups.

1. Introduction

The dynamic performance of milling processes may be analyzed by numerical, analytical, or semi-analytical techniques. Each provides a solution (or approximate solution) for the coupled, second-order, time-delay differential equations that describe the milling behavior. Research over the past several decades has shown that: 1) the milling process may be stable (i.e., forced vibration) or unstable (i.e., self-excited vibration that results in secondary Hopf bifurcations, or chatter) and; 2) the behavior depends on the selected operating parameters, typically spindle speed and axial depth of cut (for a selected radial depth) [1–17]. In a new step forward toward an increased understanding of milling dynamics, Davies et al. used once per revolution sampling to characterize the synchronicity of cutting tool motions with the tool rotation [18]. They observed the traditional secondary Hopf bifurcation, as well as period-3 tool motion (i.e., motion that repeated every three cutter revolutions) during partial radial immersion milling. Davies et al. further examined the stability of highly interrupted machining by developing a two-stage map to describe: 1) non-cutting motions governed by an analytical solution; and 2) motions during cutting using an approximation (fixed tool position with a change in momentum) [19]. They reported a doubling of the number of optimally stable spindle speeds when the time in cut is small. Experiments confirmed the new, low radial immersion best speeds. Table 1 provides a summary of related efforts that explore the complex bifurcation behavior in machining processes.

This paper builds on these prior studies by exploring period-n behavior for three specific dynamic systems: 1) strongly asymmetric; 2) symmetric; and 3) weakly asymmetric. Each corresponds to a configuration commonly observed in practice. Time domain simulation is applied to solve the coupled, second-order, time-delay differential equations of motion for the individual dynamic systems. The simulation outputs are verified with experiments and used to produce Poincaré and stability maps. These maps are presented to provide a comparison between the different setup dynamics and draw conclusions.

2. Strongly asymmetric dynamics

Because flexure-based experiments, where the workpiece is mounted on a single degree-of-freedom (SDOF) flexure, provide convenient measurement of the milling process outputs, they are a common choice for model validation [30,50]. This setup represents the case of strongly asymmetric system dynamics because the SDOF flexure is much more flexible in one Cartesian direction than the other two. Additionally, the tool point dynamics are typically selected so that the tool's lowest dynamic stiffness is much higher than the flexure's lowest dynamic stiffness.

To demonstrate bifurcation behavior for a strongly asymmetric system, the milling response was predicted using time domain simulation (see Appendix A) and validated using the flexure-based experimental configuration shown in Fig. 1. For this setup, the flexure's time dependent displacement, velocity, and acceleration during cutting were

* Corresponding author.
E-mail address: tony.schmitz@uncc.edu (T. Schmitz).

https://doi.org/10.1016/j.precisioneng.2018.08.001
Received 25 April 2018; Received in revised form 6 August 2018; Accepted 7 August 2018
Available online 14 August 2018
0141-6359/

Table 1
Prior studies of machining bifurcations [20–49].

First author	Year	Ref.	Topic
Moon	1994	[20]	The authors examined chaotic dynamics and fractals in machining.
Bukkapatnam	1995	[21]	The authors studied low-dimensional chaos in turning.
Stépán	1997	[22]	The authors examined nonlinear behavior during chatter.
Nayfey	1998	[23]	The authors applied perturbation methods to study chatter.
Minis	1998	[24]	The authors described characterized machining stability.
Moon	1998	[25]	The authors studied nonlinear dynamics and chaos in machining.
Moon	2001	[26]	The authors reviewed chaotic dynamics in machining
Zhao	2001	[27]	The authors used time domain to study milling bifurcations.
Davies	2002	[28]	The authors completed stability predictions for low radial immersion.
Mann	2003	[29]	The authors modeled the stability of up and down milling.
Mann	2003	[30]	The authors provided experimental validation of the stability model.
Campomanes	2003	[31]	The authors used time domain simulation to predict low radial immersion milling behavior.
Insperger	2003	[32]	The authors reported multiple chatter frequencies that may be exhibited in milling.
Insperger	2004	[33]	The authors confirmed the predictions from Davies et al.
Mann	2004	[34]	The authors modeled and verified bifurcations in milling.
Merdol	2004	[35]	The authors provided an analytical solution for low radial immersion milling stability.
Govekar	2005	[36]	The authors studied low radial immersion stability in milling.
Gradišek	2005	[37]	The authors provided stability predictions for milling.
Mann	2005	[38]	The authors studied milling bifurcations in the presence of asymmetric dynamics.
Stépán	2005	[39]	The authors modeled and verified nonlinear dynamics in milling.
Zatarain	2006	[40]	The authors studied the effect of helix angle on milling stability.
Insperger	2006	[41]	The authors included helix angle effects in milling stability maps.
Patel	2008	[42]	The authors predicted period-2 islands in milling stability maps.
Schmitz	2009	[43]	The authors provided an overview of low radial immersion behavior and demonstrated time domain milling simulation techniques.
Moradi	2014	[44]	The authors considered tool wear and process damping in milling bifurcation behavior.
Honeycutt	2015	[45]	The authors described the extended milling bifurcation diagram.
Honeycutt	2016	[46]	The authors experimentally verified time domain predictions of higher-order period-n behavior in milling.
Honeycutt	2016	[47]	The authors established a new metric for identifying milling stability.
Honeycutt	2017	[48]	The authors used subharmonic sampling to identify period-n behavior automatically in time domain milling simulation.
Honeycutt	2017	[49]	The authors predicted and measured surface location error and surface roughness under period-2 bifurcation conditions in milling.

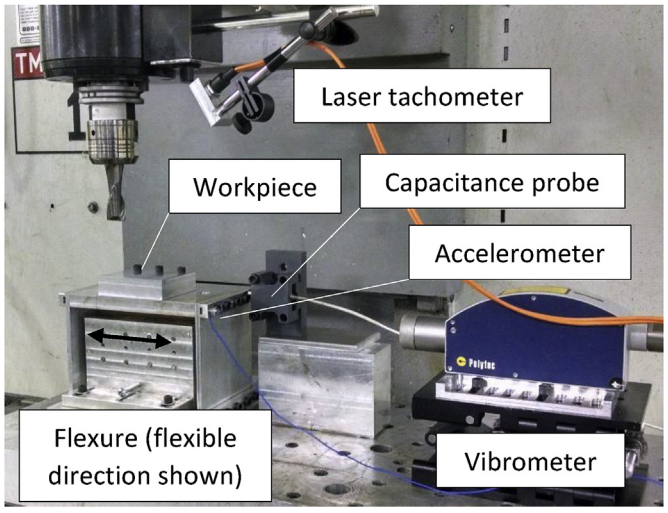

Fig. 1. SDOF parallelogram, leaf-type flexure experimental setup.

measured by a capacitance probe, laser vibrometer, and low mass accelerometer, respectively, to assess milling behavior under various process parameters. The laser tachometer signal was used to synchronously sample the flexure motion data.

The flexure and tool point dynamics are listed in Table 2. These modal parameters were extracted from (feed) and y direction impact tests completed on both the flexure and single-flute 19.05 mm diameter, 30 deg helix endmill. The mechanistic cutting force coefficients for the 6061-T6 aluminum workpiece[1] were k_{tc} = 792 N/mm^2, k_{nc} = 352 N/mm^2, k_{te} = 26 N/mm, and k_{ne} = 28 N/mm; see Appendix A for a description of the force model. Time domain simulations were completed

[1] 6061-T6 aluminum was selected, in part, to minimize the influence of tool wear on the experimental results.

Table 2
Modal parameters (natural frequency, dimensionless viscous damping ratio, and stiffness) for strongly asymmetric flexible feed direction experimental setup.

Flexure			Tool point		
x (feed direction)			x		
130.0 Hz	0.0147	2.1×10^6 N/m	1055 Hz	0.045	4.2×10^7 N/m
y			y		
756 Hz	0.085	7.7×10^7 N/m	1055 Hz	0.045	4.2×10^7 N/m

for up milling in the flexure's low stiffness direction with a 2 mm radial depth and 0.1 mm/tooth feed. The simulation outputs included the cutting force and flexure motion x and x y components for a range of {spindle speed, axial depth} combinations. The flexure displacement and velocity signals were synchronously sampled at the tooth period (once-per-revolution for the single flute cutter). Fig. 2 shows the flexure's time dependent, feed direction displacement, x, and velocity, $\frac{dx}{dt}$, as well the periodic sampling result (circles). It is observed that the process behavior repeats each period for the stable {3400 rpm, 6 mm axial depth} cut after the initial transients have attenuated.

To more effectively visualize the process behavior, the displacement is plotted versus the velocity in Fig. 3 Poincaré map. Here, the sampled points (circles) all align at a single location because the stable milling process exhibits forced vibration at the tooth period. For this figure, the transient portion (during the cut entry) was excluded to leave only the steady-state behavior.

Figs. 4 and 5 show the results for {3310 rpm, 6 mm axial depth}. This behavior represents a period-2 bifurcation because the motion repeats every other tooth period, rather than every tooth period. Here, two points are observed in the Poincaré map. Cutting tests were completed on Fig. 1 setup to validate the time domain predictions. The experimental results are presented in Fig. 6, where the displacement was measured by the capacitance probe and the velocity by the laser vibrometer. The time dependent signals were sampled once per tooth

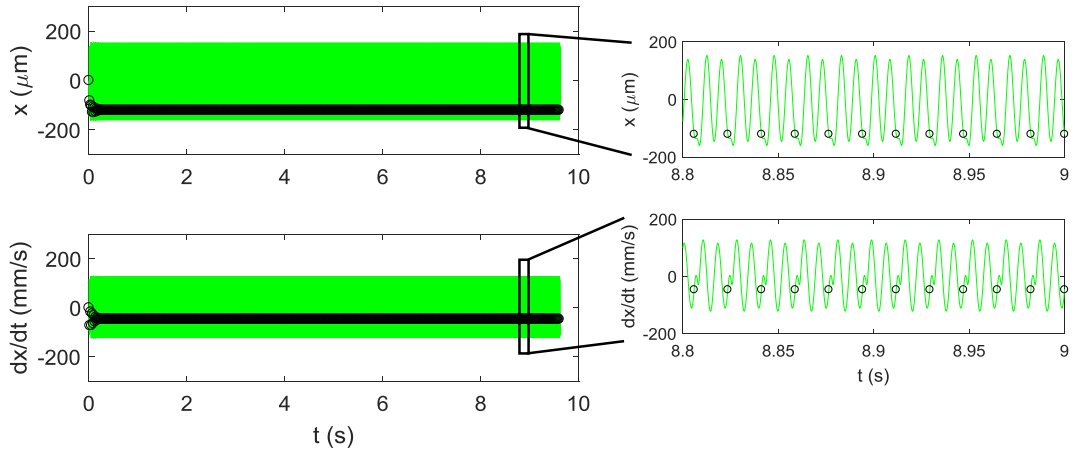

Fig. 2. Predictions for stable {3400 rpm, 6 mm axial depth} up milling using Table 2 dynamics with a 2 mm radial depth and 0.1 mm/tooth feed. (Top) time dependent displacement with periodic samples (circles); (bottom) time dependent velocity with periodic samples. (Inset) higher magnification view to observe individual periodic samples of the displacement (top) and velocity (bottom).

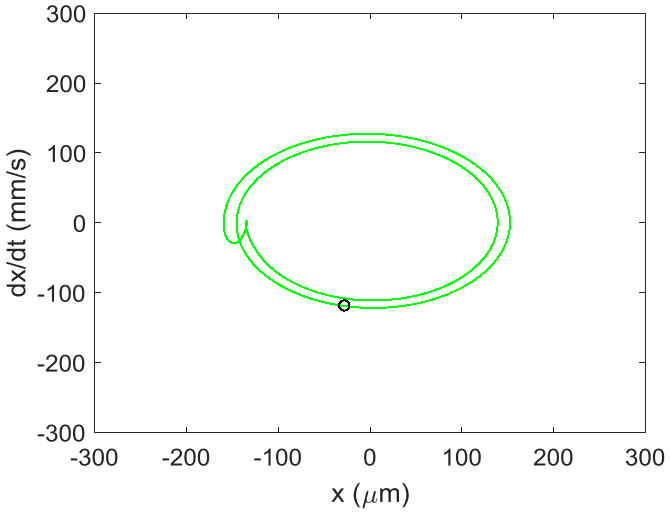

Fig. 3. Predicted Poincaré map for stable {3400 rpm, 6 mm axial depth} up milling using Table 1 dynamics with a 2 mm radial depth and 0.1 mm/tooth feed.

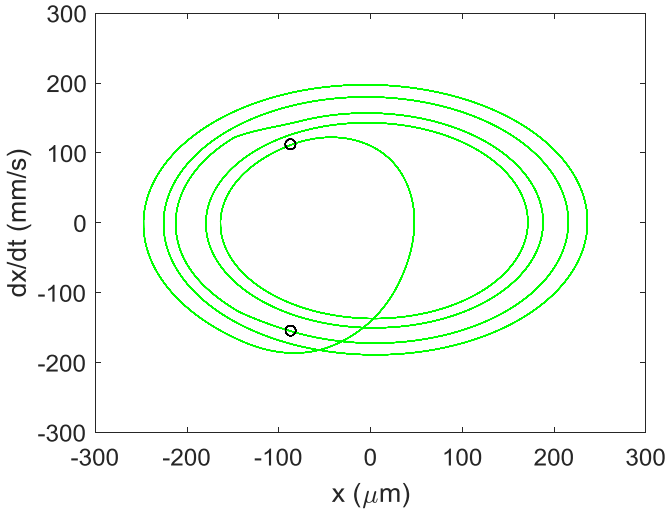

Fig. 5. Predicted Poincaré map for period-2 {3310 rpm, 6 mm axial depth} up milling using Table 2 dynamics with a 2 mm radial depth and 0.1 mm/tooth feed.

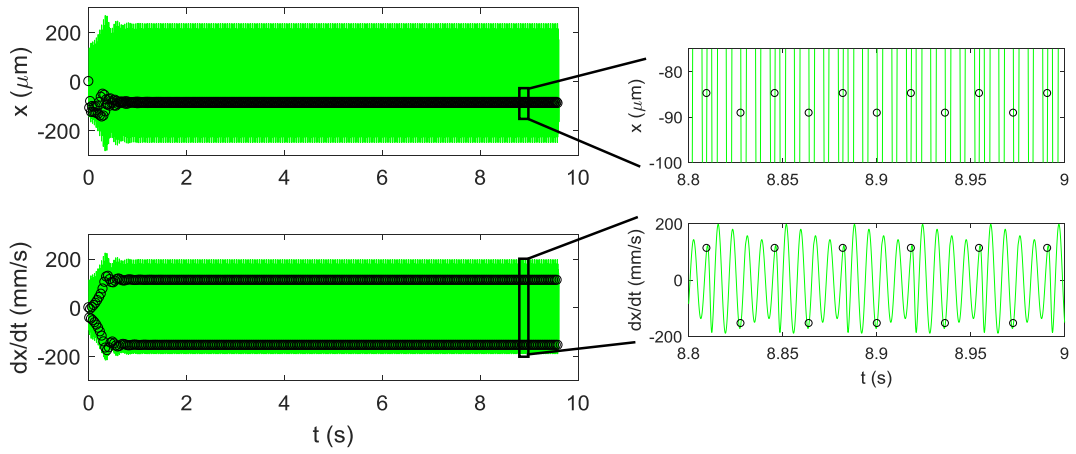

Fig. 4. Predictions for period-2 {3310 rpm, 6 mm axial depth} up milling using Table 2 dynamics with a 2 mm radial depth and 0.1 mm/tooth feed. (Top) time dependent displacement with periodic samples; (bottom) time dependent velocity with periodic samples. (Inset) higher magnification view to observe individual periodic samples of the displacement (top) and velocity (bottom).

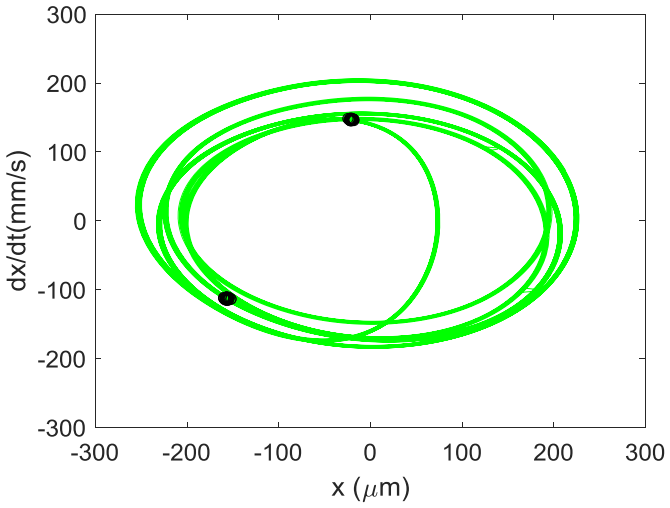

Fig. 6. Experimental Poincaré map for period-2 {3310 rpm, 6 mm axial depth} up milling using Table 2 dynamics with a 2 mm radial depth and 0.1 mm/tooth feed.

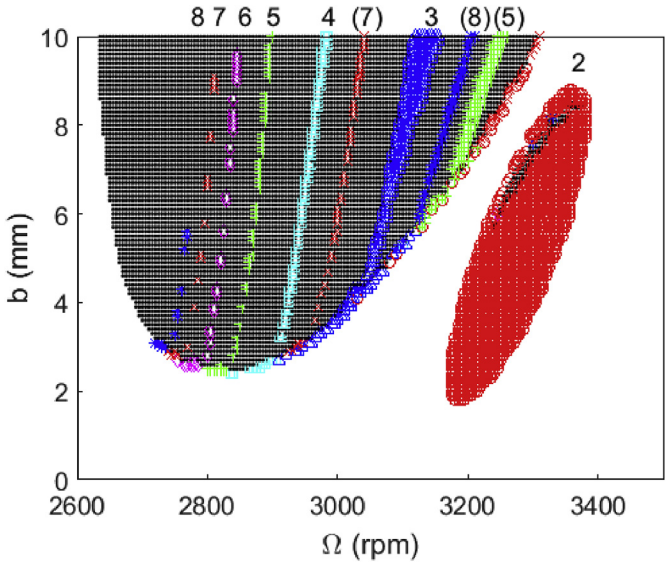

Fig. 7. Predicted stability map for up milling using Table 2 dynamics with a 2 mm radial depth and 0.1 mm/tooth feed. The bifurcation period is identified by the numerals 2–8.

Table 3
Symbols for period-n stability maps.

Period	Symbol	Color
2	Circle	Red
3	^	Blue
4	Square	Cyan
5	+	Green
6	Diamond	Magenta
7	×	Red
8	*	Blue
Stable	No symbol	(White space)
Secondary Hopf	·	Black

period using the laser tachometer signal and the transients (from the cut entry) were excluded. Good agreement with Fig. 5 is observed and the simulation performance is verified.

To obtain a global stability map, time domain simulations were completed over a grid of spindle speeds, Ω, from 2600 rpm to 3500 rpm

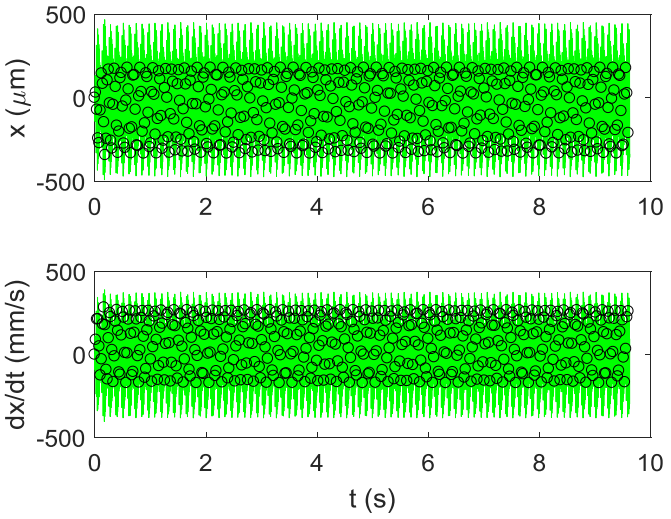

Fig. 8. Predictions for unstable {2850 rpm, 6 mm axial depth} up milling using Table 2 dynamics with a 2 mm radial depth and 0.1 mm/tooth feed. (Top) time dependent displacement with periodic samples; (bottom) time dependent velocity with periodic samples.

(5 rpm increments) and axial depths, b, from 0.1 mm to 10 mm (0.1 mm increments). Periodic sampling was applied to the x data to individually identify period-2 through period-8 bifurcations; see Appendix B for a description of the subharmonic sampling technique. The results are presented in Fig. 7, where the symbols are defined in Table 3. An elliptical, period-2 "island" is seen between 3200 rpm and 3400 rpm within the stable zone; Fig. 5 prediction and Fig. 6 experiment were completed at a point inside this island. Period-2 through period-8 bifurcation "bands" are also observed within the secondary Hopf bifurcation zone (i.e., traditional regenerative chatter). In Fig. 7, the bifurcation period is identified using the numbers 2–8, which appear at decreasing spindle speeds (i.e., right to left from 2 to 8). Repeated bands at higher speeds are also present; these are indicated with parentheses (e.g., (7) appears between 3 and 4 at a higher spindle speed range than 7).

Using Fig. 7, various bifurcation behaviors can be identified and then studied individually. For example, a secondary Hopf bifurcation is observed at {2850 rpm, 6 mm axial depth}. This quasi-periodic behavior is displayed in Fig. 8 (time domain) and Fig. 9 (Poincaré map). In

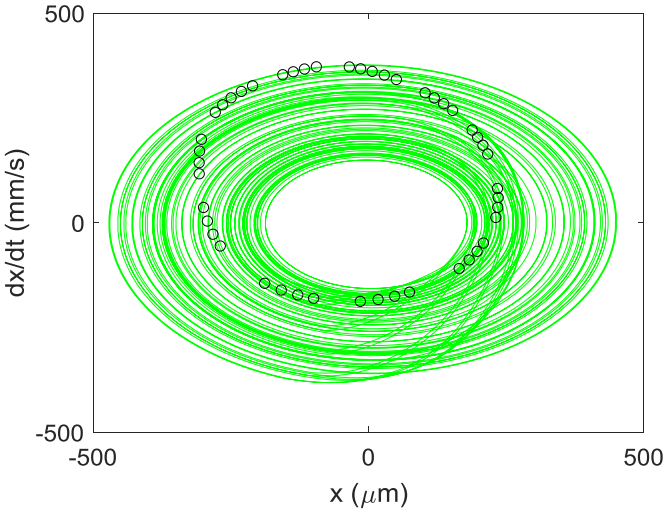

Fig. 9. Predicted Poincaré map for unstable {2850 rpm, 6 mm axial depth} up milling using Table 2 dynamics with a 2 mm radial depth and 0.1 mm/tooth feed.

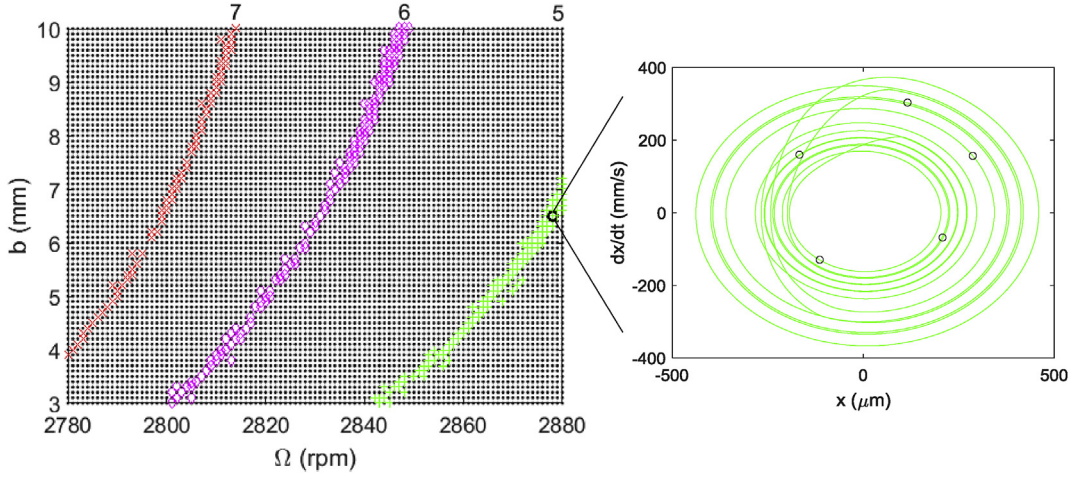

Fig. 10. High resolution predicted stability map for up milling using Table 2 dynamics with a 2 mm radial depth and 0.1 mm/tooth feed. (Inset) period-5 bifurcation example at {2878 rpm, 6.5 mm axial depth}.

Fig. 9, the characteristic elliptical distribution for the periodically sampled points is obtained due to the presence of the new incommensurate chatter frequency (i.e., self-excited vibration).

A higher resolution stability map is presented in Fig. 10 for a range of spindle speeds from 2780 rpm to 2880 rpm (1 rpm increments) and axial depths from 3 mm to 10 mm (0.1 mm increments). This shows that the apparently discontinuous period-n bands from Fig. 7 are actually continuous; the bands are simply narrow relative to the original 5 rpm resolution. A period-5 example for {2878 rpm, 6.5 mm axial depth} is provided in the inset.

A similar SDOF flexure-based setup, but with slightly different flexible direction dynamics, was tested next; see Table 4. The stability map is provided in Fig. 11 for up milling in the flexible direction with a radial depth of 5 mm and feed of 0.1 mm/tooth (5 rpm and 0.1 mm increments). The mechanistic cutting force coefficients for the 6061-T6 aluminum workpiece were again $k_{tc} = 792\,\text{N/mm}^2$, $k_{nc} = 352\,\text{N/mm}^2$, $k_{te} = 26\,\text{N/mm}$, and $k_{ne} = 28\,\text{N/mm}$ and the same single-flute 19.05 mm diameter, 30 deg helix tool was used. The behavior is similar to Fig. 7, but the period-2 island is condensed to points along the stable-secondary Hopf boundary between 4000 rpm and 4200 rpm for the new system dynamics. Validation for a point in the period-3 zone at {3800 rpm, 4.5 mm axial depth} is included in Figs. 12 and 13. Good agreement is again observed between prediction and experiment.

Given the experimental validation of the time domain simulation (Figs. 1, 5 and 62-13), it was then exercised to evaluate the effects of changes in the system dynamics on the milling process behavior. For example, Fig. 14 shows the stability map for Table 4 dynamics, but with a reduced damping ratio for the flexible direction of the SDOF flexure. The new damping ratio is 50% smaller than the original (0.0054 compared to 0.0108). It is seen that the period-2 island is now present and is again accompanied by additional period-n behavior within the secondary Hopf zone. The inset shows the stable boundary that encompasses all bifurcation types for clarity. Period-2 behavior exists within the narrow island between 4000 rpm and 4200 rpm.

Next, rather than milling in the flexible (x) direction for the strongly

Table 4
Modal parameters for strongly asymmetric flexible feed direction experimental setup.

Flexure			Tool point		
x (feed direction)			x		
163.0 Hz	0.0108	5.6×10^6 N/m	1055 Hz	0.045	4.2×10^7 N/m
y			y		
756 Hz	0.085	7.7×10^7 N/m	1055 Hz	0.045	4.2×10^7 N/m

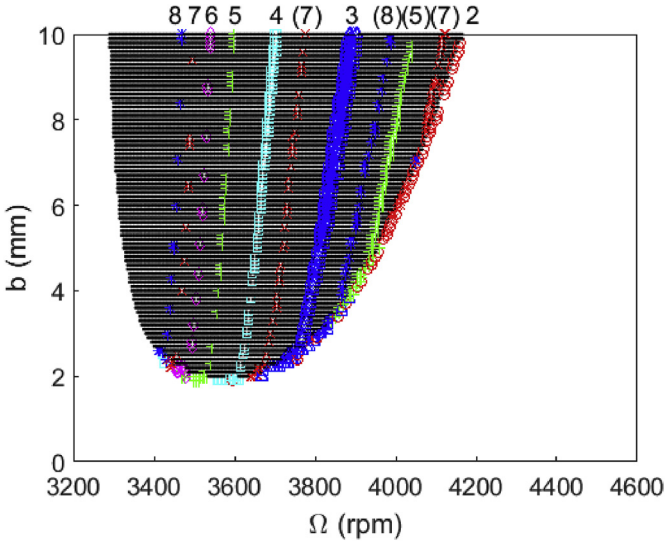

Fig. 11. Predicted stability map for up milling using Table 4 dynamics with a 5 mm radial depth and 0.1 mm/tooth feed.

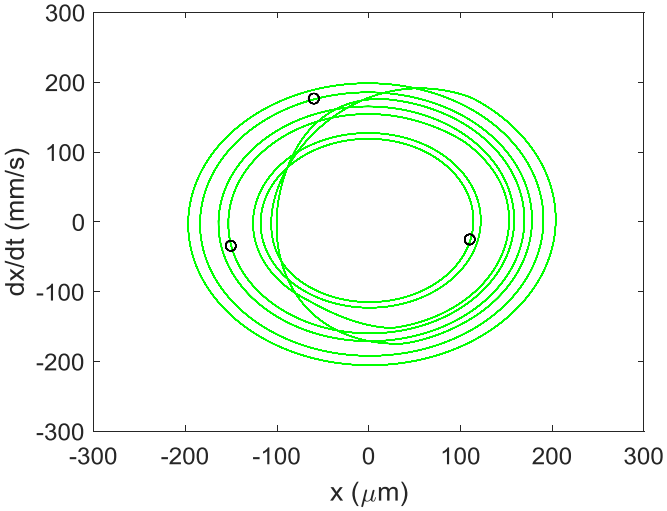

Fig. 12. Predicted Poincaré map for period-3 {3800 rpm, 4.5 mm axial depth} up milling using Table 4 dynamics with a 5 mm radial depth and 0.1 mm/tooth feed.

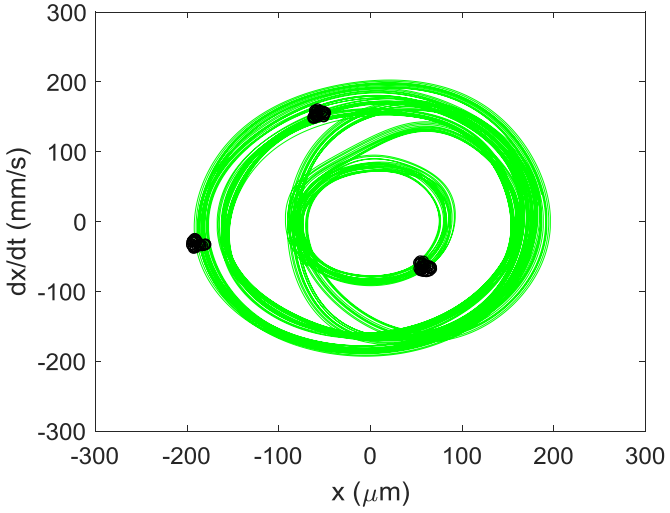

Fig. 13. Experimental Poincaré map for period-3 {3800 rpm, 4.5 mm axial depth} up milling using Table 4 dynamics with a 5 mm radial depth and 0.1 mm/tooth feed.

asymmetric flexure-based setup, the feed direction was the stiff (y) direction. The flexure and tool point dynamics are listed in Table 5 for up milling with a radial depth of 2 mm and 0.35 mm/tooth feed. Here, the mechanistic cutting force coefficients (6061-T6 aluminum workpiece) were $k_{tc} = 770\,\text{N/mm}^2$, $k_{nc} = 368\,\text{N/mm}^2$, $k_{te} = 22\,\text{N/mm}$, and $k_{ne} = 22\,\text{N/mm}$ for a new single-insert 19.05 mm diameter, 0 deg helix tool. The stability map is displayed in Fig. 15 (5 rpm and 0.1 mm increments). A significant secondary Hopf unstable zone is observed within the larger period-2 island. Experimental validations for two points within the stability map are presented in Figs. 16 and 17 (stable {3600 rpm, 5 mm axial depth}) and Figs. 18 and 19 (period-2 {3180 rpm, 5 mm axial depth}). Good agreement is observed in both cases.

3. Symmetric dynamics

Because tools, holders, and spindles are rotationally symmetric by design, it is common to observe symmetric system dynamics in practice. Therefore, simulations were next completed using the validated time domain solution to see how the process behavior changed with a shift from strongly asymmetric to symmetric dynamics. First, Table 2 dynamics were modified to match the flexure's stiff y direction modal parameters to the flexible x direction; see Table 6. The same cutting force model and cutting conditions as used for Fig. 7 were applied. A comparison of the symmetric and strongly asymmetric stability maps is provided in Fig. 20 (5 rpm and 0.1 mm increments). It is seen that: 1) the period-2 island has expanded into the original secondary Hopf zone; and 2) a "hump" has appeared in the stability boundary near {3100 rpm, 2 mm axial depth}.

Table 5
Modal parameters for strongly asymmetric, stiff feed direction experimental setup.

Flexure			Tool point		
x			x		
125.8 Hz	0.0136	1.75×10^6 N/m	1188 Hz	0.095	4.24×10^7 N/m
y (feed direction)			y		
756 Hz	0.085	7.7×10^7 N/m	1188 Hz	0.095	4.24×10^7 N/m

Similar behavior is observed for the stiff feed direction, strongly asymmetric setup (Table 5). Simulations were completed for symmetric dynamics, where Table 5 dynamics were modified to match the flexure's stiff y direction modal parameters to the flexible x direction; see Table 7. The same cutting force model and cutting conditions as used for Fig. 15 were selected. It is again seen that the period-2 island has migrated into the original secondary Hopf zone and a stability limit "hump" appears adjacent to the new period-2 zone. To further explore this region, a higher resolution simulation was completed for the spindle speed range from 2900 rpm to 3200 rpm (1 rpm increment) and 0.1 mm–8 mm axial depth (0.1 mm increment). The results are displayed in Fig. 22.

4. Weakly asymmetric dynamics

As a final study, Table 7 dynamic system was modified slightly to introduce weak asymmetry into the modal parameters. This is seen in practice, for example, when the flexible tool response dominates the system dynamics, but the x direction is slightly stiffer than the y (or vice versa) due to asymmetry in the spindle-machine dynamics into which the endmill is inserted. For this study, the y direction stiffness and natural frequency were set to 90% of the x (feed) direction values; see Table 8. The same cutting force model and cutting conditions as

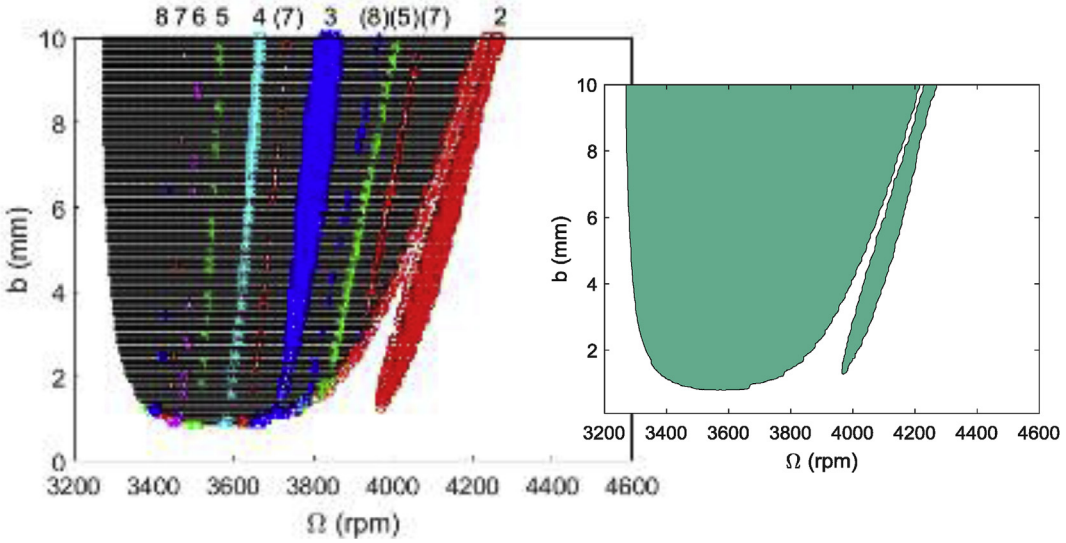

Fig. 14. Predicted stability map for up milling using Table 4 dynamics (50% reduction in flexure's x direction damping ratio) with a 5 mm radial depth and 0.1 mm/tooth feed. (Inset) stable boundary.

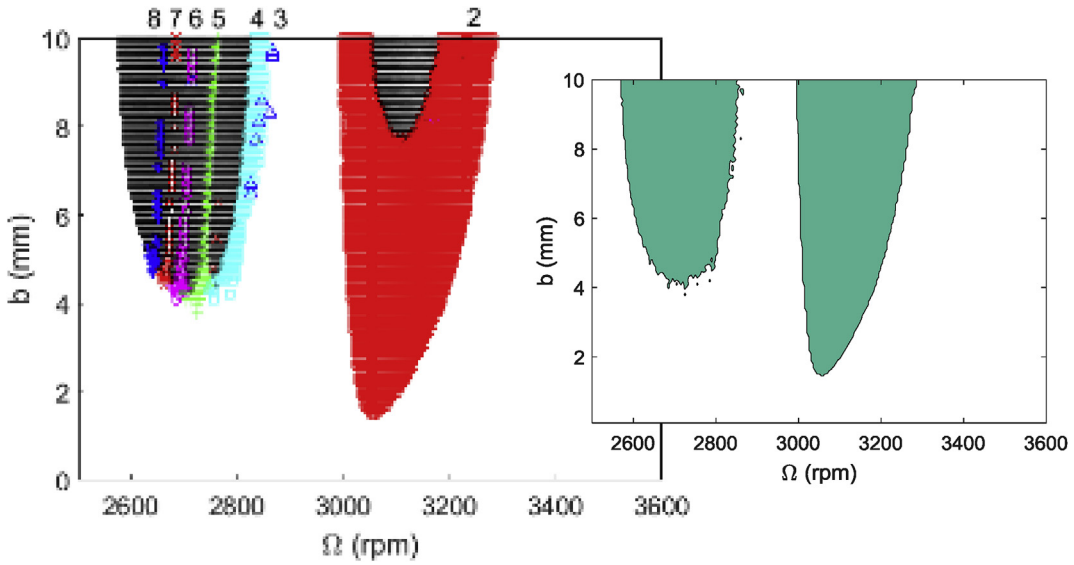

Fig. 15. Predicted stability map for up milling using Table 5 dynamics with a 2 mm radial depth and 0.35 mm/tooth feed. (Inset) stable boundary.

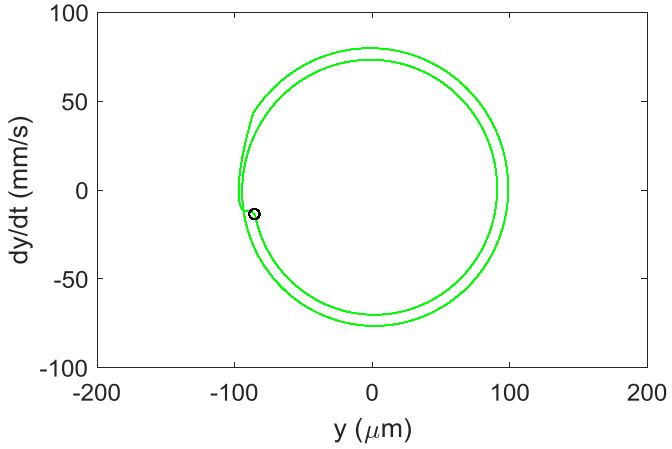

Fig. 16. Predicted Poincaré map for stable {3600 rpm, 5 mm axial depth} up milling using Table 5 dynamics with a 2 mm radial depth and 0.35 mm/tooth feed.

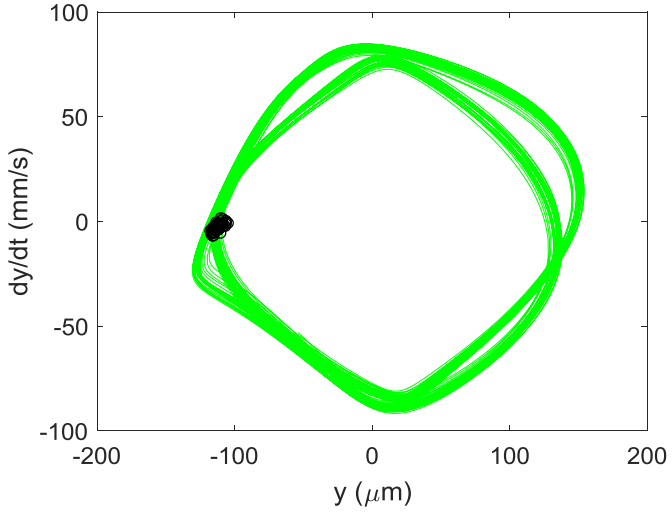

Fig. 17. Experimental Poincaré map for stable {3600 rpm, 5 mm axial depth} up milling using Table 5 dynamics with a 2 mm radial depth and 0.35 mm/tooth feed.

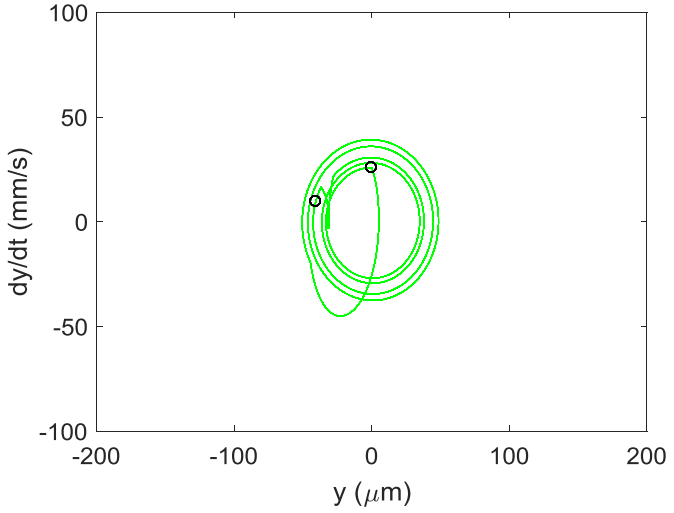

Fig. 18. Predicted Poincaré map for period-2 {3180 rpm, 5 mm axial depth} up milling using Table 5 dynamics with a 2 mm radial depth and 0.35 mm/tooth feed.

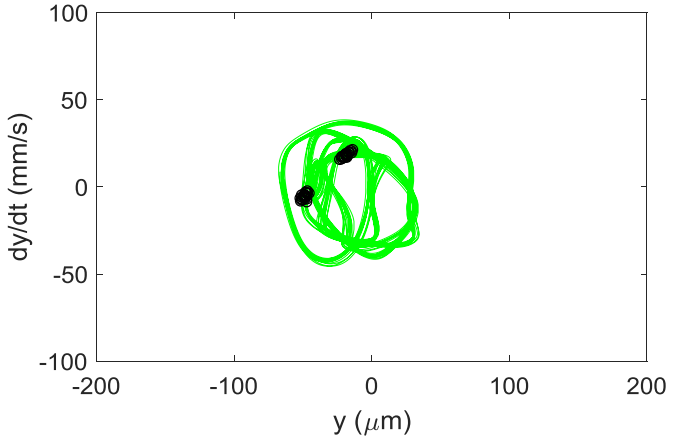

Fig. 19. Experimental Poincaré map for period-2 {3180 rpm, 5 mm axial depth} up milling using Table 5 dynamics with a 2 mm radial depth and 0.35 mm/tooth feed.

Table 6
Modal parameters for symmetric dynamics system (modification of Table 2 dynamics).

Flexure			Tool point		
x (feed direction)			x		
130.0 Hz	0.0147	2.1×10^6 N/m	1055 Hz	0.045	4.2×10^7 N/m
y			y		
130.0 Hz	0.0147	2.1×10^6 N/m	1055 Hz	0.045	4.2×10^7 N/m

Table 7
Modal parameters for symmetric dynamics system (modification of Table 5 dynamics).

Flexure			Tool point		
x			x		
125.8 Hz	0.0136	1.75×10^6 N/m	1188 Hz	0.095	4.24×10^7 N/m
y			y		
125.8 Hz	0.0136	1.75×10^6 N/m	1188 Hz	0.095	4.24×10^7 N/m

Table 8
Modal parameters for weakly asymmetric dynamics system (modification of Table 7 dynamics).

Flexure			Tool point		
x (feed)			x		
125.8 Hz	0.0136	1.75×10^6 N/m	1188 Hz	0.095	4.24×10^7 N/m
y			y		
0.9 (125.8) Hz	0.0136	0.9 (1.75×10^6) N/m	1188 Hz	0.095	4.24×10^7 N/m

used for Figs. 15 and 21 were again applied. The results are displayed in Fig. 23, where it is seen that the stable gap (white space) has shifted, the period-2 island appears within the stable zone, and the stability hump has grown to a local stability peak (near 2900 rpm) with a new period-2 zone immediately to its left. Clearly, the weak asymmetry has added significant complexity to the overall stability behavior.

5. Conclusions

This paper described the application of time domain simulation to the prediction of milling behavior for strongly asymmetric, symmetric, and weakly asymmetric system dynamics. These choices correspond to three common physical setups: a single degree-of-freedom flexure setup often used to perform validation experiments (strongly asymmetric); long, flexible endmill dynamics (symmetric); and tool or workpiece-dominated dynamics with slight asymmetry in the plane of the cut (weakly asymmetric). The time domain simulation outputs included displacement and velocity, which were synchronously sampled to identify the milling behavior. The two signals were sampled at the tooth period to produce Poincaré maps. Also, subharmonic periodic sampling was completed at integer multiples of the tooth period and then these results were combined with a numerical stability metric to automatically produce a stability map from a grid of time domain simulations. Experimental validation was provided for the flexure-based setups. The following results were observed.

- Strongly asymmetric dynamics

In a first flexure-based setup (Table 2), the process behavior was predicted and verified for feed in the flexible direction of the asymmetric flexure. A period-2 island was seen in the stable zone with period-3 and higher bands located within the traditional secondary Hopf bifurcation zone. In a second flexure-based setup (Table 4), the process behavior was again predicted and verified for feed in the flexible direction. In this case, the period-2 island did not appear, but was predicted for lower damping in the flexible direction. For a third flexure-based setup (Table 5), the feed was in the stiff direction. A larger period-2 island was present, but a significant secondary Hopf zone also appeared within the island. The period-3 and higher bands were again seen within the traditional secondary Hopf bifurcation zone.

- Symmetric dynamics

The dynamics for the first and third flexure-based setups were modified to match both directions to the original flexible direction. Time domain simulations were completed to produce stability maps for the two cases. It was seen that the period-2 island expanded into the original secondary Hopf zone and a hump appeared in the stability boundary near the new period-2 location in both instances. The period-3 and higher bands persisted.

- Weakly asymmetric dynamics

The third flexure-based setup dynamics were modified to be weakly asymmetric. Here, the original stiff direction was modified to be similar to the flexible direction, but not identical (the stiffness and natural frequency were set to 90% of the flexible direction values). It was seen in the stability map that the stable gap shifted in spindle speed, a

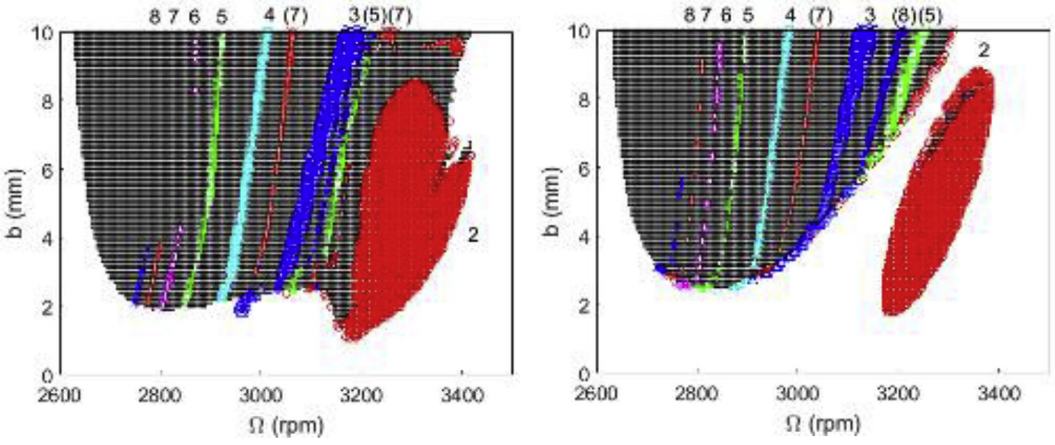

Fig. 20. Predicted stability map for up milling using Tables 2 and 6 dynamics with a 2 mm radial depth and 0.1 mm/tooth feed. (Left) symmetric, Table 6 dynamics; (right) strongly asymmetric, Table 2 dynamics.

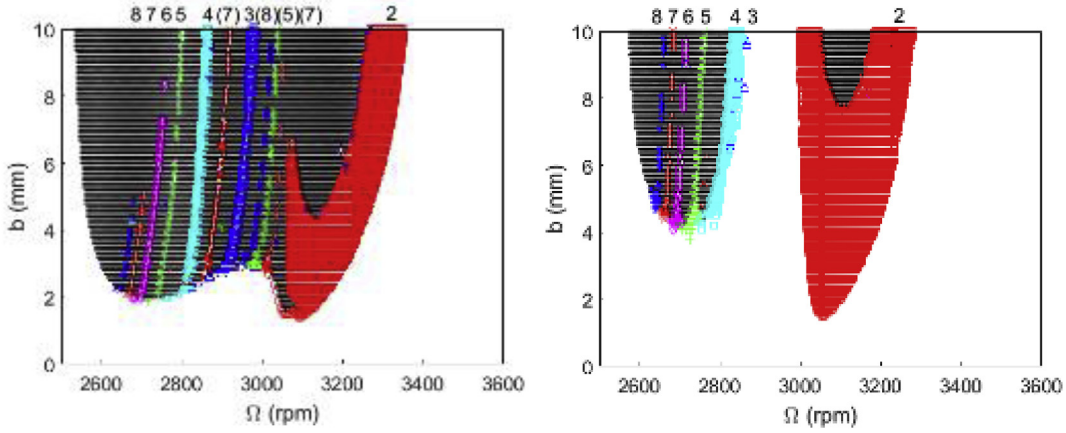

Fig. 21. Predicted stability map for up milling using Tables 5 and 7 dynamics with a 2 mm radial depth and 0.35 mm/tooth feed. (Left) symmetric, Table 7 dynamics; (right) strongly asymmetric, Table 5 dynamics with stiff direction feed.

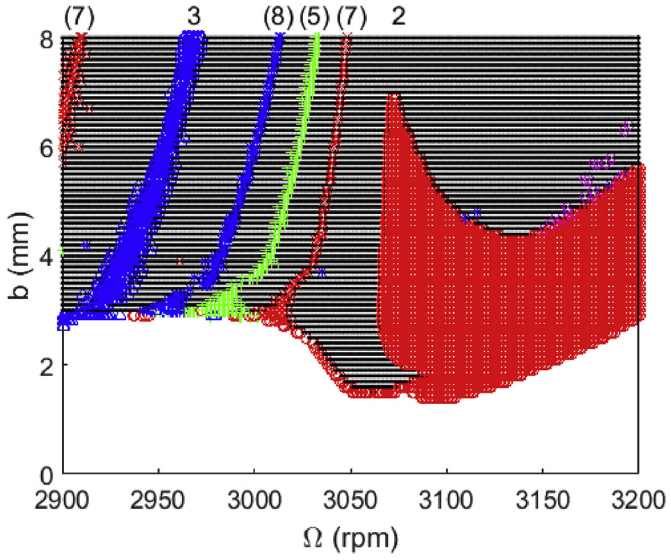

Fig. 22. High resolution predicted stability map for up milling using Table 7 symmetric dynamics with a 2 mm radial depth and 0.35 mm/tooth feed.

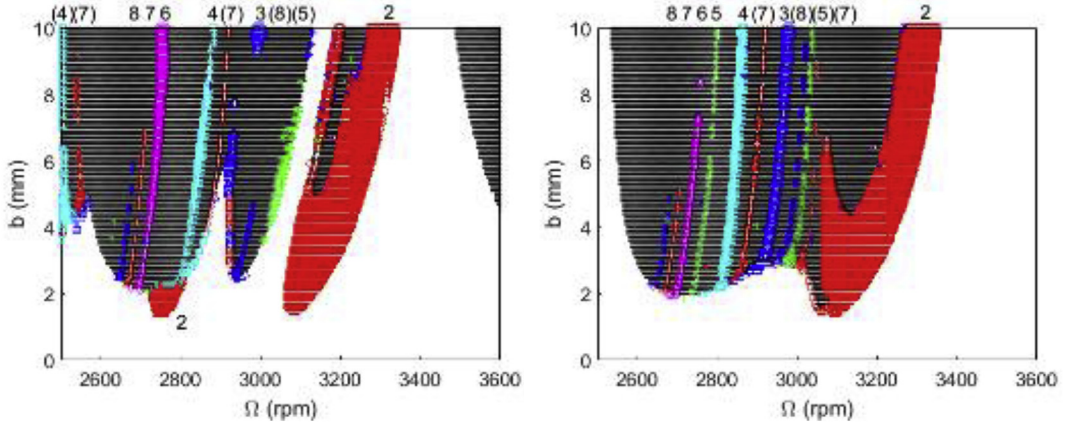

Fig. 23. Predicted stability map for up milling using Tables 7 and 8 dynamics with a 2 mm radial depth and 0.35 mm/tooth feed. (Left) weakly asymmetric, Table 8 dynamics; (right) symmetric, Table 7 dynamics.

period-2 island appeared within the stable zone, and a new local stability peak with a corresponding period-2 zone appeared. Generally speaking, the weak asymmetry added significant complexity to the stability map.

Acknowledgements

This material is based on work supported by the National Science Foundation under Grant No. CMMI-1561221. The authors also gratefully acknowledge helpful discussions with Drs. J. Ziegert and M. Davies, UNC Charlotte.

Appendix A. Time domain simulation description

Time domain simulation enables the numerical solution of the coupled, second-order, time-delay equations of motion for milling in small time steps [43]. It is well-suited to incorporating all the intricacies of milling dynamics, including the nonlinearity that occurs if the tooth leaves the cut due to large amplitude vibrations and complicated tool geometries (including runout, or different radii, of the cutter teeth, non-proportional teeth spacing, and variable helix). The simulation is based on the Regenerative Force, Dynamic Deflection Model described by Smith and Tlusty [51]. As opposed to stability maps that provide a global picture of the stability behavior, time domain simulation provides information regarding the local cutting force and vibration behavior for the selected cutting conditions. The simulation used in this study proceeds as follows (see Fig. A1):

1. The instantaneous chip thickness, $h(t)$, is determined using the vibration of the current and previous teeth at the selected tooth angle
2. The cutting force components in the tangential (t) and normal (n) directions are calculated using:

$$F_t(t) = k_{tc} b h(t) + k_{te} b$$
$$F_n(t) = k_{nc} b h(t) + k_{ne} b, \tag{A1}$$

where b is the axial depth of cut and the cutting force coefficients are identified by the subscripts t or n for direction and c or e for cutting or edge effect. The reader may note that the axial force component was not considered. This is justified by the significantly higher stiffness along the tool axis relative to the lateral directions.

3. The force components are used to find the new displacements by numerical solution of the differential equations of motion in the x and y directions:

$$m_x \ddot{x} + c_x \dot{x} + k_x x = F_t(t)\cos(\phi) + F_n \sin(\phi)$$
$$m_y \ddot{y} + c_y \dot{y} + k_y y = F_t(t)\sin(\phi) - F_n \cos(\phi), \tag{A2}$$

where m is the modal mass, c is the modal viscous damping coefficient, and k and the modal stiffness. The subscripts identify the direction and multiple degrees of freedom in each direction can be accommodated.

4. The tool rotation angle is incremented and the process is repeated.

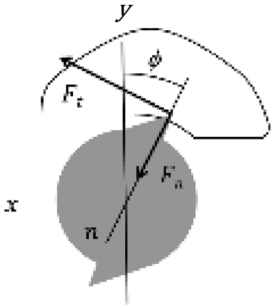

Fig. A1. Cutting force geometry. The normal and tangential direction cutting forces, F_n and F_t, are displayed. The fixed x (feed) and y directions, as well as the rotating normal direction, n, are also shown. The angle ϕ defines the tooth angle. The tool feed is to the right for the clockwise tool rotation and the axial depth is in the z direction.

The instantaneous chip thickness depends on the nominal, tooth angle-dependent chip thickness, the current vibration in the direction normal to the surface, and the vibration of previous teeth at the same angle. The chip thickness can be expressed using the circular tooth path approximation as:

$$h(t) = f_t \sin(\phi) + n(t - \tau) - n(t), \tag{A3}$$

where f_t is the commanded feed per tooth, ϕ is the tooth angle, n is the normal direction (see Fig. A1), and τ is the tooth period. The tooth period is defined as:

$$\tau = \frac{60}{\Omega N_t}(\text{sec}), \tag{A4}$$

where Ω is the spindle speed in rpm and N_t is the number of teeth. The vibration in the direction of the surface normal for the current tooth depends on the x and y vibrations as well as the tooth angle according to:

$$n = x \sin(\phi) - y \cos(\phi). \tag{A5}$$

For the simulation, the strategy is to divide the angle of the cut into a discrete number of steps. At each small time step, dt, the cutter angle is incremented by the corresponding small angle, $d\phi$. This approach enables convenient computation of the chip thickness for each simulation step because: 1) the possible teeth orientations are predefined; and 2) the surface created by the previous teeth at each angle may be stored. The cutter

rotation:

$$d\phi = \frac{360}{SR}(\text{deg}) \tag{A6}$$

depends on the selection of the number of steps per revolution, SR. The corresponding time step is:

$$dt = \frac{60}{SR \cdot \Omega}(\text{sec}) \tag{A7}$$

A vector of angles is defined to represent the potential orientations of the teeth as the cutter is rotated through one revolution of the circular tool path, $\phi = [0, d\phi, 2d\phi, 3d\phi, \ldots, (SR-1)d\phi]$. The locations of the teeth within the cut are then defined by referencing entries in this vector.

In order to accommodate the helix angle for the tool's cutting edges, the tool may be sectioned into a number of axial slices. Each slice is treated as an individual straight tooth endmill, where the thickness of each slice is a small fraction, db, of the axial depth of cut, b. Each slice incorporates a distance delay:

$$r\chi = db\,\tan(\gamma) \tag{A8}$$

relative to the prior slice (nearer the cutter free end), which becomes the angular delay between slices:

$$\chi = \frac{db\,\tan(\gamma)}{r} = \frac{2db\,\tan(\gamma)}{d}(\text{rad}) \tag{A9}$$

for the rotating endmill, where d is the endmill diameter and γ is the helix angle. In order to ensure that the angles for each axial slice match the predefined tooth angles, the delay angle between slices is:

$$\chi = d\phi. \tag{A10}$$

This places a constraint on the db value. By substituting $d\phi$ for χ and rearranging, the required slice width is:

$$db = \frac{d \cdot d\phi}{2\,\tan(\gamma)}. \tag{A11}$$

This simple description can be extended to include:

1. Multiple tool modes – the x and y forces are used to calculate the acceleration, velocity, and displacement for each tool mode (represented by the modal parameters) and the results are summed in each direction
2. Flexible workpiece – the x and y forces are also used to determine the workpiece deflections, again by numerical integration, and the relative tool-workpiece vibration is used to calculate the instantaneous chip thickness
3. Runout of the cutter teeth – the chip thickness is updated by the runout of the current tooth
4. Unequal teeth spacing – the tooth angle vector is modified to account for the actual tooth pitch.

Appendix B. Periodic sampling description

To construct a stability map using time domain simulation, a separate simulation is completed at each position in the desired grid of {spindle speed, axial depth} values. A primary challenge in this approach, however, is automatically establishing the stability limit using the predicted time domain signals. As described in Refs. [47,48], a stability criterion based on the periodically sampled data may be implemented. The stability metric for sampling at the tooth period is:

$$M1 = \frac{\sum_{i=2}^{N} |x_{s1}(i) - x_{s1}(i-1)|}{N}, \tag{B1}$$

where x_{s1} is the vector of once per tooth sampled x displacements and N is the length of the x_{s1} vector. Other variables, such as y displacement or cutting force may be selected as well. With this stability metric, the absolute value of the differences in successive sampled points is summed and then normalized. The sampled points repeat for a stable cut, so the $M1$ value is ideally zero. For unstable cuts, on the other hand, $M1 > 0$, due to the asynchronous motion in secondary Hopf instability and jumps from one fixed point to the next in period-n bifurcations.

Periodic sampling at the tooth period, τ, enables stable and unstable zones to be identified, but this approach does not distinguish between secondary Hopf and period-n instabilities. However, using subharmonic sampling at $n\tau$ (n = 2, 3, 4, …), the corresponding period-n bifurcations can be separately established. For example, when sampling at 2τ, the stability metric becomes “blind” to period-2 bifurcations. The metric for this case is:

$$M2 = \frac{\sum_{i=2}^{N} |x_{s2}(i) - x_{s2}(i-1)|}{N}, \tag{B2}$$

where x_{s2} is the vector of x displacements sampled once every other tooth period (i.e., a 2τ sampling period), and N is the length of the x_{s2} vector. Generically, the metric can be expressed as shown in Eq. (B3), where the integer $n = 1, 2, 3, \ldots$defines the sampling period (i.e., $n\tau$).

$$Mn = \frac{\sum_{i=2}^{N} |x_{sn}(i) - x_{sn}(i-1)|}{N}, \tag{B3}$$

The subharmonic sampling approach is implemented to construct a stability map that individually identifies each bifurcation type. The metrics $M1$ through $M8$, which represent τ through 8τ integer sampling periods, are used to isolate the stable zone as well as the different bifurcation types: period-2, -3, -4, -5, -6, -7, -8, and secondary Hopf instability. The logic used to construct the stability map follows, where the 1 μm limit is an arbitrarily small value that indicates an approximately zero level and accounts for numerical variations due to floating point precision and Euler integration:

if $M1 \leq 1$ μm.

(stable, do nothing)

elseif $M2 \leq 1\,\mu m$.

plot a circle (period-2)

elseif $M3 \leq 1\,\mu m$.

plot a triangle (period-3)

elseif $M4 \leq 1\,\mu m$ and $M2 > 1\,\mu m$.

plot a square (period-4, excludes period-2)

elseif $M5 \leq 1\,\mu m$.

plot a + (period-5)

elseif $M6 \leq 1\,\mu m$ and $M2 > 1\,\mu m$ and $M3 > 1\,\mu m$.

plot a diamond (period-6, excludes period-2 and period-3)

elseif $M7 \leq 1\,\mu m$.

plot an × (period-7)

elseif $M8 \leq 1\,\mu m$ and $M2 > 1\,\mu m$ and $M4 > 1\,\mu m$.

plot a * (period-8, excludes period-2 and period-4)

else.

plot a dot (secondary Hopf or high order period-n)

end.

References

[1] Arnold RN. The mechanism of tool vibration in the cutting of steel. Proceedings of the institute of mechanical engineers. 1946. p. 154.
[2] Doi S, Kato S. Chatter vibration of lathe tools. Trans ASME 1956;78:1127–34.
[3] Tobias SA, Fishwick W. The chatter of lathe tools under orthogonal cutting conditions. Trans ASME 1958;80:1079–88.
[4] Tlusty J, Polacek M. The stability of machine tools against self-excited vibrations in machining,. Proceedings of the ASME international research in production engineering conference, pittsburgh, PA. 1963. p. 465–74.
[5] Tobias SA. Machine tool vibration. New York: Wiley; 1965.
[6] Merritt HE. Theory of self-excited machine-tool chatter. ASME J Eng Ind 1965;87:447–54.
[7] Tlusty J, Polacek M. Experience with analysing stability of machine tool against chatter. Proceedings of the 9th MTDR conference. 1968. p. 521–70.
[8] Shridar R, Hohn RE, Long GW. A general formulation of the milling process equation. ASME J Eng Ind 1968;90:317–24.
[9] Hohn RE, Shridar R, Long GW. A stability algorithm for a special case of the milling process. ASME J Eng Ind 1968;90:326–9.
[10] Shridar R, Hohn RE, Long GW. A stability algorithm for the general milling process. ASME J Eng Ind 1968;90:330–4.
[11] Hanna NH, Tobias SA. A theory of nonlinear regenerative chatter. J Eng Ind 1974;96:247–55.
[12] Tlusty J, Ismail F. Basic non-linearity in machining chatter. Ann CIRP 1981;30:299–304.
[13] Tlusty J, Ismail F. Special aspects of chatter in milling. ASME J Vib, Stress Reliab Des 1983;105:24–32.
[14] Tlusty J. Machine dynamics. In: King RI, editor. Handbook of high-speed machining technology. New York: Chapman and Hall; 1985. p. 48–153.
[15] Tlusty J. Dynamics of high-speed milling. ASME J Eng Ind 1986;108:59–67.
[16] Minis I, Yanusevsky R. A new theoretical approach for prediction of chatter in milling. ASME J Eng Ind 1993;115:1–8.
[17] Altintas Y, Budak E. Analytical prediction of stability lobes in milling. Ann CIRP 1995;44(1):357–62.
[18] Davies MA, Dutterer BS, Pratt JR, Schaut AJ. On the dynamics of high-speed milling with long, slender endmills. Ann CIRP 1998;47(1):55–60.
[19] Davies MA, Pratt JR, Dutterer BS, Burns TJ. The stability of low radial immersion milling. Ann CIRP 2000;49(1):37–40.
[20] Moon FC. Chaotic dynamics and fractals in material removal processes. In: Thompson J, Bishop S, editors. Nonlinearity and chaos in engineering dynamics. Wiley; 1994. p. 25–37.
[21] Bukkapatnam S, Lakhtakia A, Kumara S. Analysis of senor signals shows turning on a lathe exhibits low-dimensional chaos. Phys Rev E 1995;52:2375–87.
[22] Stépán G, Kalmár-Nagy T. Nonlinear regenerative machine tool vibrations. Proceedings of the 1997 ASME design engineering technical conference on vibration and noise, Sacramento, CA. 1997. p. 1–11. DETC 97/VIB-4021.
[23] Nayfey A, Chin C, Pratt J. Applications of perturbation methods to tool chatter dynamics. In: Moon FC, editor. Dynamics and chaos in manufacturing processes. Wiley; 1998. p. 193–213.
[24] Minis I, Berger BS. Modelling, analysis, and characterization of machining dynamics. In: Moon FC, editor. Dynamics and chaos in manufacturing processes. Wiley; 1998. p. 125–63.
[25] Moon FC, Johnson M. Nonlinear dynamics and chaos in manufacturing processes. In: Moon FC, editor. Dynamics and chaos in manufacturing processes. Wiley; 1998. p. 3–32.
[26] Moon FC, Kalmár-Nagy T. Nonlinear models for complex dynamics in cutting materials. Phil Trans Roy Soc Lond 2001;359:695–711.
[27] Zhao MX, Balachandran B. Dynamics and stability of milling process. Int J Solid Struct 2001;38:2233–48.
[28] Davies MA, Pratt JR, Dutterer B, Burns TJ. Stability prediction for low radial immersion milling. J Manuf Sci Eng 2002;124:217–25.
[29] Mann BP, Insperger T, Bayly PV, Stépán G. Stability of up-milling and down-milling, Part 1: alternative analytical methods. Int J Mach Tool Manufact 2003;43(1):25–34.
[30] Mann BP, Insperger T, Bayly PV, Stépán G. Stability of up-milling and down-milling, Part 2: experimental verification. Int J Mach Tool Manufact 2003;43(1):35–40.
[31] Campomanes ML, Altintas Y. An improved time domain simulation for dynamic milling at small radial immersions. J Manuf Sci Eng 2003;125(3):416–22.
[32] Insperger T, Stépán G, Bayly PV, Mann BP. Multiple chatter frequencies in milling processes. J Sound Vib 2003;262:333–45.
[33] Insperger T, Stépán G. Vibration frequencies in high-speed milling processes or A positive answer to Davies, Pratt, Dutterer, and Burns. J Manuf Sci Eng 2004;126(3):481–7.
[34] Mann BP, Bayly PV, Davies MA, Halley JE. Limit cycles, bifurcations, and accuracy

of the milling process. J Sound Vib 2004;277:31–48.
[35] Merdol SD, Altintas Y. Multi frequency solution of chatter stability for low immersion milling. J Manuf Sci Eng 2004;126:459–66.
[36] Govekar E, Gradišek J, Kalveram M, Insperger T, Weinert K, Stepan G, Grabec I. On stability and dynamics of milling at small radial immersion. Ann CIRP 2005;54(1):357–62.
[37] Gradišek J, Kalveram M, Insperger T, Weinert K, Stépán G, Govekar E, Grabec I. On stability prediction for milling. Int J Mach Tool Manufact 2005;45(7–8):769–81.
[38] Mann BP, Garg NK, Young KA, Helvey AM. Milling bifurcations from structural asymmetry and nonlinear regeneration. Nonlinear Dynam 2005;42(4):319–37.
[39] Stépán G, Szalai R, Mann BP, Bayly PV, Insperger T, Gradisek J, Govekar E. Nonlinear dynamics of high-speed milling – analyses, numerics, and experiments. J Vib Acoust 2005;127:197–203.
[40] Zatarain M, Muñoa J, Peigné G, Insperger T. Analysis of the influence of mill helix angle on chatter stability. Ann CIRP 2006;55(1):365–8.
[41] Insperger T, Munoa J, Zatarain MA, Peigné G. Unstable islands in the stability chart of milling processes due to the helix angle,. CIRP 2nd international conference on high performance cutting, Vancouver, Canada, June. 2006. p. 12–3.
[42] Patel BR, Mann BP, Young KA. Uncharted islands of chatter instability in milling. Int J Mach Tool Manufact 2008;48(1):124–34.
[43] Schmitz T, Smith KS. Machining dynamics: frequency response to improved productivity. New York, NY: Springer; 2009.
[44] Moradi H, Vossoughi G, Movahhedy M. Bifurcation analysis of nonlinear milling process with tool wear and process damping: sub-harmonic resonance under regenerative chatter. Int J Mech Sci 2014;85:1–19.
[45] Honeycutt A, Schmitz T. The extended milling bifurcation diagram. Procedia Manuf 2015;1:466–76.
[46] Honeycutt A, Schmitz T. A numerical and experimental investigation of period-n bifurcations in milling. J Manuf Sci Eng 2016;139/1:011003.
[47] Honeycutt A, Schmitz T. A new metric for automated stability identification in time domain milling simulation. J Manuf Sci Eng 2016;138/7:074501.
[48] Honeycutt A, Schmitz T. Milling stability interrogation by subharmonic sampling. J Manuf Sci Eng 2017;139/4:041009.
[49] Honeycutt A, Schmitz T. Surface location error and surface roughness for period-n milling bifurcations. J Manuf Sci Eng 2017;139/6:061010.
[50] Ransom T, Honeycutt A, Schmitz T. A new tunable dynamics platform for milling experiments. Precis Eng 2016;44:252–6.
[51] Smith KS, Tlusty J. An overview of modeling and simulation of the milling process. J Eng Ind 1991;113:169–75.